Liu *et al. Geoscience Letters* (2023) 10:60
https://doi.org/10.1186/s40562-023-00315-5

Geoscience Letters

RESEARCH LETTER

Open Access

Improved Indian Ocean dipole seasonal prediction in the new generation of CMA prediction system

Bo Liu[1,3,4], Kai Yang[2,5*], Xiangwen Liu[1,3,4], Gang Huang[2] and Benjamin Ng[5]

Abstract

Seasonal prediction of the Indian Ocean dipole (IOD) is important, considering its impact on the climate of surrounding regions. Here we compare the prediction of the IOD in two generations of prediction system developed by the China Meteorology Administration (CMA), i.e., the second-generation climate model prediction system (CPSv2) and CPSv3. The results show that CPSv3 has better ability to predict the variability and spatial pattern of the IOD than CPSv2, especially when the lead time is long. CPSv3 maintains a certain level of credibility when predicting IOD events with 6-month lead time. The improved data assimilation in CPSv3 has reduced the predictability error of eastern Indian Ocean sea surface temperature (SST) and contributed to improvements in IOD prediction. Enhanced simulation of the El Niño-Southern Oscillation (ENSO)–IOD relationship promotes better prediction skill of ENSO-related IOD events in CPSv3. Our results suggest that upgrading data assimilation and the simulation of the ENSO–IOD relationship are critical for improving the prediction of the IOD in coupled climate models.

Keywords Indian Ocean dipole, Seasonal prediction, Climate extremes, Climate models

Introduction

The Indian Ocean dipole (IOD) is the dominate sea surface temperature (SST) anomaly pattern in the tropical Indian Ocean in June–July–August (JJA) and September–October–November (SON) (Saji et al. 1999; Webster et al. 1999). During its positive phase, cool SST anomalies in the southeast tropical Indian Ocean and warm SST anomalies in the west force a northwestward shift of atmospheric convection, inducing opposite rainfall anomalies in regions around the western and eastern Indian Ocean (Behera et al. 2005; Cai et al. 2009; Yang et al. 2020). A positive IOD can develop more strongly than a negative IOD resulting in stronger impacts on the climate of Indian Ocean-rim countries (Cai et al. 2021; Ummenhofer et al. 2009; Yang et al. 2020). For example, the 2019 extreme positive IOD caused floods in East Africa which affected more than 2.8 million people and devastating bushfires in Australia where more than 3000 buildings were destroyed and a burnt area of more than 170,000 km^2 (Wang et al. 2020).

Extreme positive IOD events are projected to occur more frequently in a warming climate (Cai et al. 2014, 2021). Thus, improvement in the seasonal prediction of the IOD is required to minimize its impacts and damages. Considerable effort has been made to predict the IOD using coupled climate models (e.g., Liu et al. 2017; Luo et al. 2007; Shi et al. 2012; Liu et al. 2021a, b). The IOD prediction skills of coupled models are related to the

*Correspondence:
Kai Yang
yangkai@mail.iap.ac.cn
[1] CMA Earth System Modeling and Prediction Centre (CEMC), Beijing, China
[2] State Key Laboratory of Numerical Modeling for Atmospheric Sciences and Geophysical Fluid Dynamics, Institute of Atmospheric Physics, Chinese Academy of Sciences, Beijing, China
[3] State Key Laboratory of Severe Weather (LASW), Chinese Academy of Meteorological Sciences, Beijing, China
[4] Key Laboratory of Earth System Modeling and Prediction China Meteorological Administration, Beijing, China
[5] CSIRO Environment, Aspendale, VIC, Australia

initialization, data assimilation, the performance of models in simulating the ocean–atmosphere dynamics in the tropical Indian Ocean, and the El Niño-Southern Oscillation (ENSO)–IOD relationship (Liu et al. 2017; Luo et al. 2007). The IOD and ENSO can influence the evolution of each other through ocean–atmosphere interaction in the Pacific and Indian Oceans (e.g., the Walker circulation, Cai et al. 2019; Luo et al. 2010). In some cases, accurate simulation of the ENSO–IOD relationship is the key to the prediction of extreme IOD events in coupled models (Doi et al. 2020).

The Beijing Climate Center Climate System Model (BCC-CSM), which participated in the international Coupled Model Intercomparison Project phase 5 (CMIP5) and phase 6 (CMIP6), has been widely used in the seasonal prediction of climate variability in East Asia and the tropics (Liu et al. 2015). Based on BCC-CSM1.1(m), a medium-resolution version of BCC-CSM (Wu et al. 2010), the second-generation climate model prediction system, CPSv2 was operationalized in 2016. With reasonable skill in predicting East Asian climate, CPSv2 has limited ability in predicting the IOD and its relationship with ENSO (Liu et al. 2015). In 2021, the third-generation system (CPSv3) was developed based on the high-resolution version of BCC-CSM, referred to as BCC-CSM2-HR (Liu et al. 2021a, b). With significant upgrades to its dynamical core and model physics, BCC-CSM2-HR has been demonstrated to have improved ability in simulating the inter-tropical convergence zone (ITCZ), the ENSO cycle, and the Madden–Julian Oscillation (MJO), and so on (Liang et al. 2022; Liu et al. 2021a, b). Despite a substantial improvement in model framework, how these changes will influence seasonal prediction of the IOD has not been fully assessed (Liang et al. 2022). Here we use the ensemble hindcast experiment in CPSv2 and CPSv3 during the period of 2002–2022 to evaluate their performance in seasonal prediction of the IOD.

Data and method

Model description

In BCC-CSM-1.1(m), the atmospheric component of the model utilizes the BCC Atmospheric General Circulation Model (AGCM), featuring a horizontal resolution of T106 (approximately 100 km) and 26 hybrid sigma/pressure layers in the vertical direction (Wu et al. 2010). The land component is based on version 1.0 of the BCC Atmosphere and Vegetation Interaction Model. The ocean and sea ice components are version 4 of the Geophysical Fluid Dynamics Laboratory Modular Ocean Model (MOM4; Griffies et al. 2005) and the Sea Ice Simulator (SIS4; Winton 2000), respectively. These different components are coupled without any flux adjustment.

BCC-CSM2-HR was developed for Subseasonal-to-Seasonal (S2S) and short-term forecasts. The atmospheric component of BCC-CSM2-HR is BCC-AGCM version 3 (Wu et al. 2021), with a horizontal resolution of T266 triangular truncation (approximately 45 km) and 56 vertical hybrid sigma/pressure layers, with the top level at 0.1 hPa. Some developments were made for both the dynamical core and model physics in the atmospheric components, such as a deep cumulus convection scheme, spatially varying damping for the divergence field, and modified boundary layer turbulence (Wu et al. 2021). The ocean component of BCC-CSM2-HR is updated to MOM5 (Griffies 2012), with a horizontal resolution of 0.25° and 50 vertical levels. The land component is BCC-AVIM (the Atmosphere and Vegetation Interaction Model) version 2, and the sea ice component is also updated from SIS4 to SIS5 (Delworth et al. 2006).

Experiment design

CPSv2 and CPSv3 are developed based on BCC-CSM-1.1(m) and BCC-CSM2-HR, respectively. In addition to the upgrade of the model framework, the data assimilation system is also different between these two systems. The initialization scheme in CPSv2 is a nudging method (Liu et al. 2015), where the four-times daily air temperature, winds, and surface pressure fields from the National Centers for Environmental Prediction (NCEP; Kanamitsu et al. 2002) and sea temperature from Global Ocean Data Assimilation System (GODAS) version 2 (Behringer and Xue 2004) are used.

For CPSv3, a coupled data assimilation is applied, including a based Ensemble Kalman Filter (Evensen 2003) in the ocean component, an Optimal Interpolation (IO) algorithm in the sea ice component and a multi-level nudging method in the atmosphere component. This coupled data assimilation is a more consistent data assimilation scheme and can produce a more reliable analysis than other reanalysis products (Liu et al. 2021a, b).

Historical hindcast experiments have been conducted based on the two prediction system. Each hindcast experiment in CPSv2 includes 24 members, produced by a lagged average forecasting (LAF) with a combination of different atmospheric and oceanic initial conditions at the end of the month preceding the beginning of the hindcast. This ensemble forecast initiates monthly from January 1991 to present. In CPSv3, 21 members starting once a month from January 2001 to present have been conducted. Ensemble member 0 is initialized with undisturbed initial conditions (ICs), while the remaining members undergo perturbations. These perturbations are introduced to account for the uncertainty arising from both the initial conditions and the

unresolved sub-grid-scale processes. These processes are addressed through parameterization techniques within the atmospheric model, including LAF and stochastically perturbed parameterization tendency (SPPT) schemes. Despite CPSv2 initiating its forecasting as early as January 1991, for the purpose of a more robust comparison with CPSv3, we ultimately used results from January 2002 to December 2022.

Validation data and methods

For model evaluation, we use SST data from NOAA Optimum Interpolation SST version 2 (OISST; Reynolds et al. 2002), and multi-level sea temperature data from GODAS (Behringer and Xue 2004). All the reanalysis/observations and hindcast data cover a 21-year period from 2002 to 2022 and are all interpolated onto the OISST grid before comparison. The anomalies of each variable are calculated relative to the 2002–2022 climatology.

The statistical methods employed in this study encompass regression, correlation analysis, and physical examination. The standard two-tailed Student's t-test is utilized to assess significance levels. Prediction skill and forecast error are gaged through the anomaly correlation coefficient (ACC) and root-mean-square error (RMSE), respectively. To estimate predictability error, the RMSE is calculated between each perturbed member and the ensemble mean, followed by the averaging of results from sub-samples. This measurement helps quantify the error attributable to initial condition uncertainties under a perfect-model assumption (Kim et al. 2014).

To assess the performance of the models at different forecast lead times, the concept of "lead month" is introduced. The LM## (e.g., LM00) is employed to quantify the forecast lead time, with "##" signifying the month following the initial time. For example, if the start time is 1 January, 2001, the predicted target month of January is denoted as LM00, while the subsequent month of February is designated as LM01. Unless otherwise specified, we apply the ensemble mean of the 24 (21) members in CPSv2 (CPSv3) to evaluate their prediction skill of IOD.

Results

In observations, the tropical eastern Indian Ocean has a warmer climatological SST with a deeper thermocline than the tropical western Indian Ocean (Fig. 1a). While

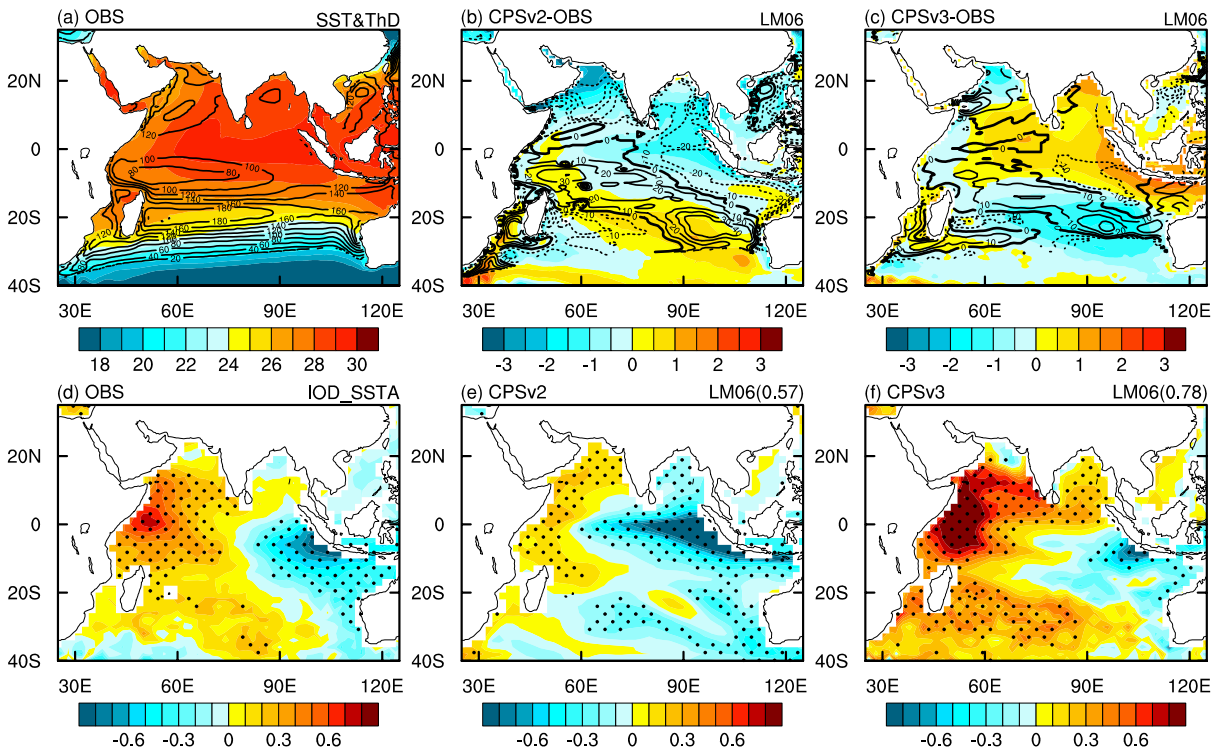

Fig. 1 Indian Ocean climatology and IOD pattern in observation and CMA prediction systems. **a** Climatology of SST (shaded) and 20 °C isotherm depth (contours) in observation. **b**, **c** Difference of the climatology of SST (shaded) and 20 °C isotherm depth (contours) between observations and predictions using **b** CPSv2 and **c** CPSv3 at 6-month lead time. **d**–**f** SST anomalies regressed onto monthly DMI over the Indian Ocean in **d** observations and **e** CPSv2 and **f** CPSv3 at 6-month lead time. The black dotted areas in **d**, **e**, **f** indicate significance above the 95% confidence level. The pattern correlation coefficients between simulated and observed IOD patterns are shown in the top right of **e**, **f**

the climatological thermocline in the eastern Indian Ocean gets deeper poleward, there is a thermocline dome in the tropical western Indian Ocean. Examining the predicted SST field at a lead time of 6 months, we find that the mean state of SST in CPSv2 tends to exhibit a cold bias over the central-eastern tropical Indian Ocean with the most cooling in the eastern region (Fig. 1b). Additionally, this cold bias is accompanied by a weak warm bias in the western part of the Indian Ocean and there is also a positive thermocline depth bias in the southwest Indian Ocean, especially in the thermocline dome. In contrast, CPSv3 shows the opposite bias of SST climatology over the tropical Indian Ocean with a more accurate simulation of the thermocline depth (Fig. 1c). CPSv2 exhibits significant biases in simulating thermocline depth in the eastern and western tropical Indian Ocean, with deviation centers of +30 m and −20 m, respectively. In contrast, CPSv3 shows substantial improvement in simulating the thermocline depth, reducing the bias centers in the eastern and western tropical Indian Ocean to around ±10 m. We also find similar improvement of thermocline simulation in the historical run of BCC-CSM2-HR. The improvement in the climatological thermocline depth of the tropical Indian Ocean enables the model to better simulate the variability of the Indian Ocean.

Due to the mean SST and equatorial easterly wind biases in CPSv2, the negative SST anomalies in the eastern Indian Ocean during a positive IOD are much stronger and extend further to the west than in observations, forcing a relatively weak warming in western Indian Ocean (Fig. 1d, e). On the other hand, CPSv3 simulates a more realistic IOD spatial pattern even though the cooling in the southeast Indian Ocean is confined to a small area off Sumatra–Java (Fig. 1f). The pattern correlation of SST anomalies associated with the IOD between observation and CMA prediction systems has improved from 0.57 in CPSv2 to 0.78 in CPSv3.

According to the ensemble mean of the hindcast experiments, CPSv3 shows better skill in the prediction of monthly DMI, which is a commonly used IOD index (Saji et al. 1999) calculated as the SST anomaly difference between the western Indian Ocean (10° S to 10° N and 50° E to 70° E) and the southeast Indian Ocean (10° S to 0° and 90° E to 110° E), than CPSv2 (Fig. 2). In the two generations of the CMA prediction systems, the correlation of observed and predicted DMI time series has increased from 0.58 to 0.69 at lead time of 2 months, from 0.42 to 0.6 at lead time of 4 months, and from 0.36 to 0.57 at lead time of 6 months. The improvement of DMI prediction from CPSv2 to CPSv3 is more significant when the lead time is longer. At a lead time of 6 months, CPSv3 has accurately predicted 2019 as the strongest positive IOD year in the past 21 years, while CPSv2 predicts 2019 as a moderate positive IOD (Fig. 2a, b). However, CPSv3 appears to underestimate the 2019 strong pIOD at a lead time of 2 months. This may be caused by the anomalously cool SST in the western Indian Ocean in July (2019) predicted by CPSv3 starting from July. In turn, the westward extension of the equatorial easterly wind is substantially blocked and this is unfavorable for the formation of the positive Bjerknes feedback and the development of strong pIOD (Additional file 1: Figure S1). The initial negative SST anomalies in the western Indian Ocean in July could potentially be associated with the data assimilation process and initial conditions. Apart from the improved prediction of the DMI, CPSv3 also shows enhanced simulation of the spatial pattern of SST anomalies associated with the IOD. The pattern correlation of the IOD SST patterns in observations and predictions has increased by 0.13, 0.28, and 0.21 (from 0.75 to 0.88, 0.60 to 0.88, 0.57 to 0.78) from CPSv2 to CPSv3 with a lead time of 2, 4, and 6 months, respectively (Additional file 1: Figure S2). In CPSv2, an IOD in its developing and mature phase can be well predicted (defined as when the ACC is larger than 0.5) with up to 3–4-month lead (Fig. 2c). While in CPSv3, skillful prediction of the IOD is found with a lead time up to 6 months (Fig. 2d).

The ensemble mean of the hindcast experiments has better DMI prediction skill than individual experiments. This is primarily attributed to the appropriate ensemble strategies employed in those forecast systems, which contributes to reducing their predictive uncertainties and is consistent with the findings of other ensemble forecast studies (e.g., Liu et al 2017; Hu et al 2014; Kumar et al 2003; Jin et al 2008). Additionally, most of the hindcast experiments in CPSv3 show higher DMI prediction skill than the hindcast experiments based on CPSv2, especially when the lead time is long (Fig. 3a, b). This demonstrates the robustness of the improvement in IOD prediction from CPSv2 to CPSv3.

We also compare the prediction skill of SST variability in the western and eastern IOD poles. This suggests that the high ACC of DMI in CPSv3 is mainly due to the improved prediction of IOD eastern pole variability (Fig. 3a, d). CPSv3 generally shows similar ACC values of IOD western pole prediction with CPSv2 (Fig. 3c). However, this does not mean that CPSv3 has no improvement over the western Indian Ocean as SST variability of the western Indian Ocean is considerably underestimated in CPSv2 (Additional file 1: Figure S3). This may be a result of the thermocline mean state bias and the depressed warming in the western Indian Ocean during positive IOD events in CPSv2 (Fig. 1). The magnitude of the predicted western Indian Ocean SST anomalies is largely underestimated in CPSv2 (Additional file 1: Figure S3). In contrast, CPSv3 provides more realistic predictions of

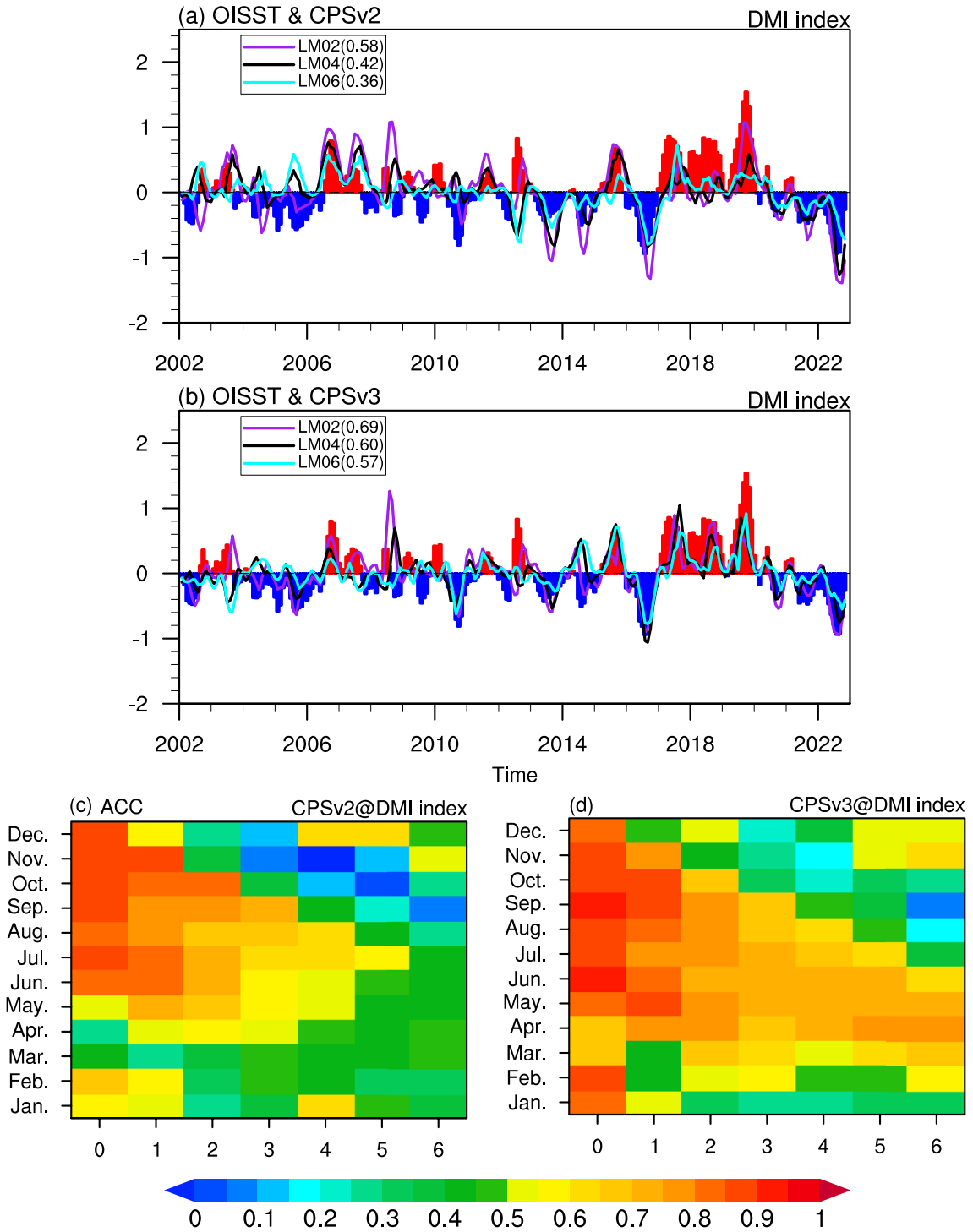

Fig. 2 Prediction of DMI in CPSv2 and CPSv3. **a**, **b** Time series of monthly DMI in observations (bars) and model ensemble mean predictions using **a** CPSv2 and **b** CPSv3 at 2- (purple line), 4- (black line) and 6-month (light-blue line) lead time from 2002 to 2022. **c**, **d** Anomaly Correlation Coefficients (ACC) of the DMI predictions using **c** CPSv2 and **d** CPSv3 as a function of lead month and different initial times. All the data have been smoothed with a 3-month running mean

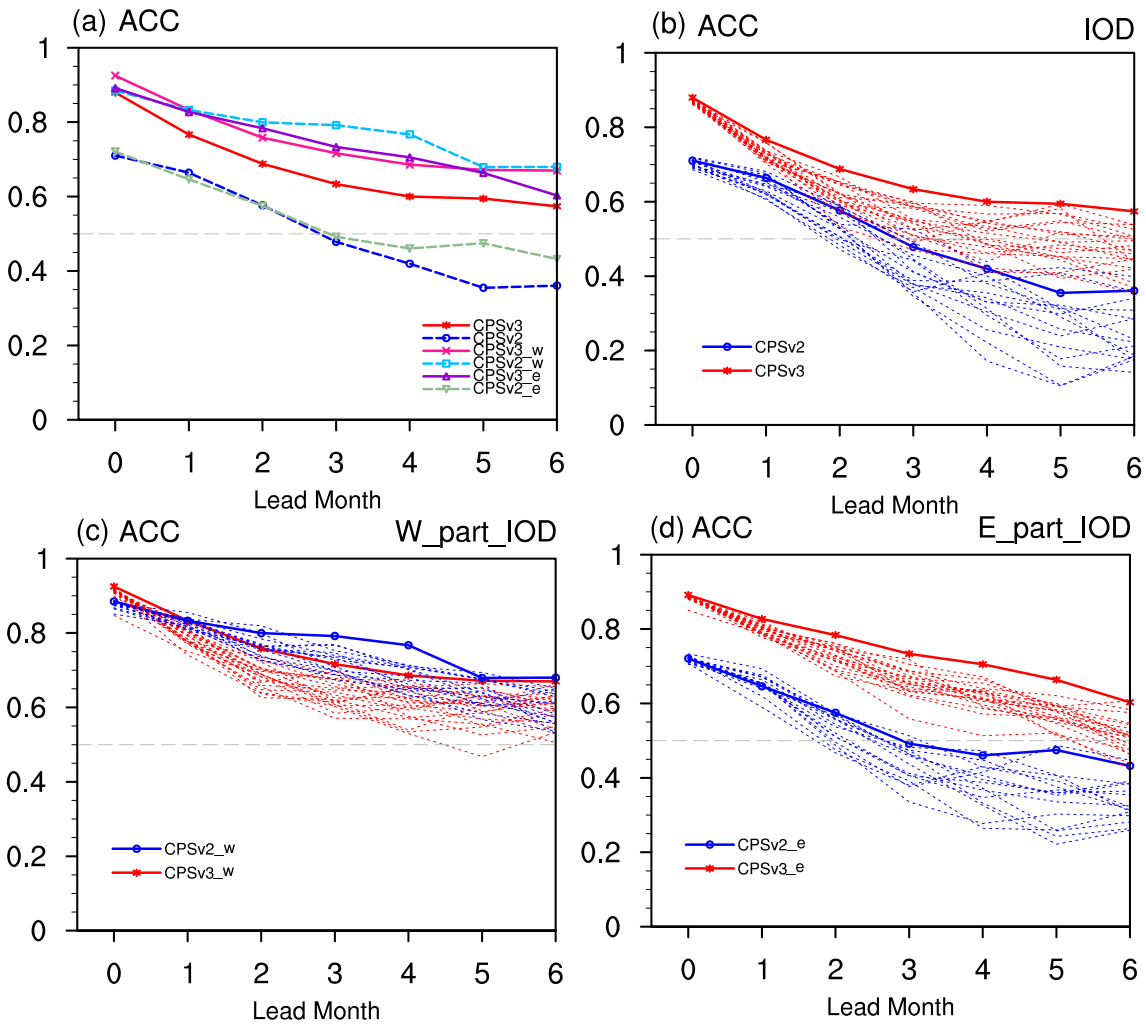

Fig. 3 Prediction of SST variability in west and east IOD poles. ACC of DMI, western pole (W), and eastern pole (E) using CPSv2 and CPSv3 predictions at different lead months. **a** represents the ensemble mean results, **b**–**d** represent the ensemble mean and the corresponding sub-samples results for **b** DMI, **c** western pole, and **d** eastern pole of DMI. The solid lines show the ensemble mean and the dotted lines show the results of each experiment. All the data have been smoothed with a 3-month running mean

the western Indian Ocean SST anomaly time series and spatial patterns of SST variability (standard deviation) in the tropical Indian Ocean. Evaluation based on RMSE shows similar results (Additional file 1: Figure S4).

We then explored the possible reasons for the improvement of IOD prediction in CPSv3. Predictability errors are used to describe the error caused by the uncertainty in the process of assimilation and initialization when treating the model as perfect. In the tropical Indian Ocean, the prediction of eastern Indian Ocean SST in CPSv2 exhibits large predictability errors increasing with the lead time (Fig. 4a). While in CPSv3, the predictability errors in the eastern Indian Ocean have been reduced. In particular, the predictability errors barely change as the lead time increases (Fig. 4b). This suggests that the upgraded data assimilation system in CPSv3 has contributed to an improved prediction skill of IOD eastern pole SST variability.

Additionally, we also compare the ENSO–IOD relationship in observations and the two CMA prediction systems. In observations, the correlation between ENSO (represented by the Niño3.4 index) and IOD increases from May and peaks in September (Fig. 4c). In SON, Niño3.4 is negatively correlated with eastern tropical Indian Ocean SST and positively correlated with the SST in the tropical west and northwest Indian Ocean (Fig. 4d). However, CPSv2 has underestimated the ENSO–IOD relationship, with an ENSO–IOD correlation coefficient close to 0 from May to November (Fig. 4c). SON SST in the Indian Ocean is either weakly correlated or

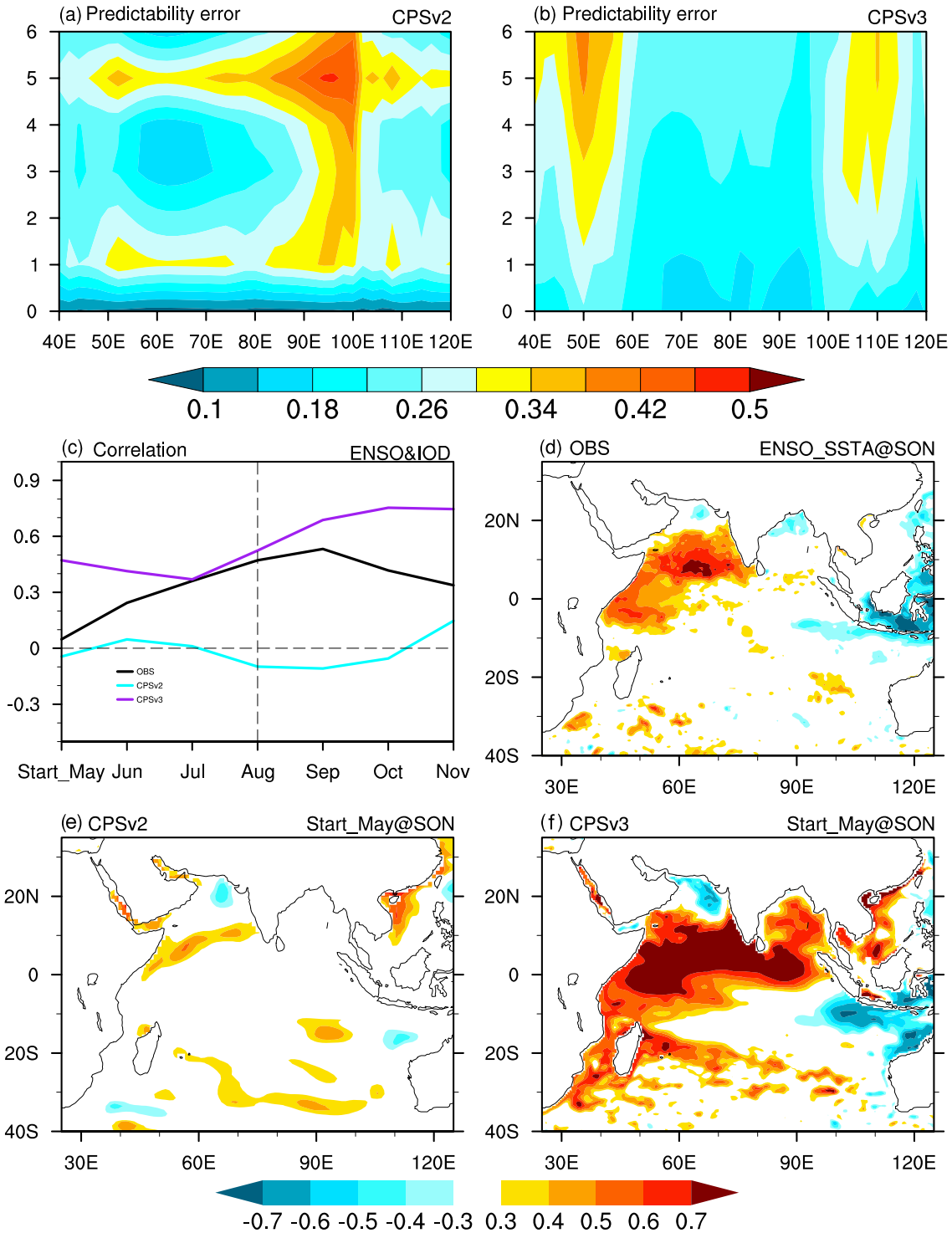

Fig. 4 Predictability errors and ENSO–IOD relationship in CPSv2 and CPSv3. Predictability errors of SST averaged over 10° S–10° N in **a** CPSv2 and **b** CPSv3 at different lead months. **c** The relationship of concurrent Niño3.4 index and DMI from May to November in observations (black line) and predictions using CPSv2 (blue line) and CPSv3 (purple line). **d**–**f** The correlation between SON Niño3.4 index and concurrent SST in the Indian Ocean in **d** observations and predictions using **e** CPSv2 and **f** CPSv3. **c**–**f** are based on predictions starting from May

not related with Niño3.4 in CPSv2 (Fig. 4e). In contrast, CPSv3 captures the Niño3.4–DMI relationship well from May to November, although the correlation in CPSv3 is stronger than that in observations (Fig. 4c, f). The more realistic ENSO–IOD relationship in CPSv3 contributes to a higher prediction skill of ENSO-related IOD in CPSv3 than in CPSv2. The improvement is more significant when the lead time is longer (Additional file 1: Figure S5). In addition, the better simulation of the relationship between ENSO and western Indian Ocean SST may contribute to more realistic western Indian Ocean SST variability in CPSv3 (Additional file 1: Figure S3). We also compare the ENSO–IOD relationship in the historical simulation of BCC-CSM.1.1(m) (used in CPSv2) and BCC-CSM2-HR (used in CPSv3), in which no data assimilation is used (Additional file 1: Figure S6). Although the correlation patterns are slightly different to that in hindcast experiments (Fig. 4), the conclusion remains consistent. BCC-CSM2-HR reproduces the ENSO–Indian Ocean SST relationship in observations well, especially for the significant positive correlation between ENSO and the tropical western Indian Ocean (Additional file 1: Figure S6). This suggests that the improved ENSO–IOD relationship and ENSO-related IOD prediction skill in CPSv3 are not attributed to data assimilation, but rather result from improvements in model dynamics.

Conclusions and discussion

In this study, we have comprehensively evaluated seasonal prediction of the IOD in two generations of CMA climate prediction systems based on ensemble hindcast experiments. The results show that the newest CPSv3 has a substantially improved prediction skill of the IOD in terms of its spatial pattern and interannual variability than its previous version, CPSv2. The total predictability of IOD events can be extended up to 6 months in advance. Specifically, CPSv2 shows an east cold-west warm mean state bias over the tropical Indian Ocean, which leads to a westward extending cooling in the eastern Indian Ocean and weak warming in the western Indian Ocean during positive IOD events. This mean state bias also contributes to underestimated SST variability in the western tropical Indian Ocean. CPSv3 better captures the spatial pattern of the IOD with a more realistic SST variability pattern simulation in the western tropical Indian Ocean. However, the mean state bias in CPSv3 also results in the cool anomalies associated with positive IODs confined to a smaller area off Sumatra–Java.

The ensemble mean of hindcast experiments shows better prediction skill than most individual hindcast experiments, and the prediction of DMI and IOD spatial patterns is better in CPSv3 than in CPSv2. The improvement is more significant when the lead time is longer. The improved prediction of DMI in CPSv3 is mainly related to the upgraded data assimilation which substantially reduces predictability errors in the eastern tropical Indian Ocean.

Furthermore, CPSv3 shows a better ability to capture the observed ENSO–IOD relationship than CPSv2. The more realistic ENSO–IOD relationship in CPSv3 has contributed to a higher prediction skill of ENSO-related IOD events compared to CPSv2. This improvement is also more significant when the lead time is longer. A better relationship between ENSO and western Indian Ocean SST also leads to a more realistic simulation of SST variability in the western Indian Ocean in CPSv3. This finding aligns with the conclusions of previous researchers using statistical methods (e.g., Zhao et al. 2019, who argued that the poor simulation of the relationship between ENSO and IOD by models is a major reason for the low skill in IOD prediction. They used a simple statistical model to correct the ENSO–IOD relationship in dynamical models, resulting in a better skill in IOD prediction. Through extensive model enhancements and improved initialization schemes, the latest prediction system, CPSv3, can accurately capture this underlying relationship and ultimately enhance IOD prediction skill.

Supplementary Information

The online version contains supplementary material available at https://doi.org/10.1186/s40562-023-00315-5.

Additional file 1: Figure S1. The Indian Ocean SST and 850-hPa wind anomalies from July to September 2019 in (a) Observations, (b) CPSv2 predicted from July 2019, and (c) CPSv3 predicted from July 2019. **Figure S2.** Indian Ocean SST anomalies regressed onto the DMI in (a, b, c) CPSv2 and (d, e, f) CPSv3 at (a, d) 2-month, (b, e) 4-month and (c, f) 6-month lead time. The black dotted areas are above the 95% significance level. The pattern correlation coefficients between predictions and observations are shown in the top right. **Figure S3.** Standard deviation map of SON SST over the Indian Ocean in (a) observations, predictions using (b) CPSv2 and (c) CPSv3. Panel (d, e) represent the time series of the DMI western pole at each month based on the OISSTv2 observations (bars; d, e) and model ensemble mean predictions using (d) CPSv2 and (e) CPSv3 at 2- (purple line), 4- (black line) and 6-month (light-blue line) lead time from 2002 to 2022. **Figure S4.** RMSE of the DMI, western pole, and eastern pole of DMI predictions using CPSv2 and CPSv3 at different lead months. (a) represents the ensemble mean results, (b, c, d) represent the ensemble mean and the corresponding sub-sample results for the DMI (b), western pole (c), and eastern pole (d) of DMI. The solid lines show the ensemble mean and the dotted lines show the results of each experiment. **Figure S5.** Correlation coefficient of DMI between observations and real-time (solid line) predictions, as well as under ENSO conditions (dotted line, calculated using linear regression, only signals related to Nino3.4 are retained in the time series of each lead month, and then the prediction skill of the IOD is calculated for different lead months.) using CPSv2 (red line) and CPSv3 (blue line). **Figure S6.** Regression of concurrent SON SST over the Indian Ocean against the Nino3.4 index in (a) observations and simulations (b) using BCC-CSM1.1(m) and (c) BCC-CSM2-HR. The black dotted areas are above the 95% significance level.

Acknowledgements
The authors thank NOAA PSL, Boulder, Colorado, USA for providing the OISSTv2 and GODAS dataset.

Author contributions
BL and KY conceived the study and wrote the initial manuscript in discussion with all the other authors. BL contributed to the data analysis and generated all the figures. All the authors contributed to interpreting results, discussion, and revision of this paper.

Funding
This work is supported by the National Key R&D Program of China (2022YFC3004200), the Youth Fund of CMA Earth System Modeling and Prediction Centre (CEMC-QNJJ-2022002), the National Natural Science Foundation of China (42105032), and China Postdoctoral Science Foundation (2018M640168).

Availability of data and materials
This work used the OISSTv2 (available at https://psl.noaa.gov/data/gridded/data.noaa.oisst.v2.highres.html) and GODAS (available at https://cfs.ncep.noaa.gov/cfs/godas/monthly/) datasets. The hindcast experiment results of CPSv2 and CPSv3 used in the study are available at https://doi.org/https://doi.org/10.5281/zenodo.8357574.

Declarations

Competing interests
Not applicable.

Received: 10 October 2023 Accepted: 30 November 2023
Published online: 11 December 2023

References

Behera SK, Luo J-J, Masson S et al (2005) Paramount impact of the Indian Ocean dipole on the East African short rains: a CGCM study. J Clim 18:4514–4530. https://doi.org/10.1175/JCLI3541.1
Behringer D, Xue Y (2004) Eighth Symposium on integrated observing and assimilation systems for atmosphere, oceans, and land surface, AMS 84th Annual Meeting, Washington State Convention and Trade Center, Seattle. Wash Am Meteor Soc 23:11–15
Cai W, Cowan T, Raupach M (2009) Positive Indian Ocean Dipole events precondition southeast Australia bushfires. Geophys Res Lett 36:L19710. https://doi.org/10.1029/2009GL039902
Cai W, Santoso A, Wang G et al (2014) Increased frequency of extreme Indian Ocean Dipole events due to greenhouse warming. Nature 510:254–258. https://doi.org/10.1038/nature13327
Cai W, Wu L, Lengaigne M et al (2019) Pantropical climate interactions. Science 363:eaav4236. https://doi.org/10.1126/science.aav4236
Cai W, Yang K, Wu L et al (2021) Opposite response of strong and moderate positive Indian Ocean Dipole to global warming. Nat Clim Chang 11:27–32. https://doi.org/10.1038/s41558-020-00943-1
Delworth TL, Broccoli AJ, Rosati A et al (2006) GFDL's CM2 global coupled climate models. Part I: formulation and simulation characteristics. J Clim 19:643–674. https://doi.org/10.1175/JCLI3629.1
Doi T, Behera SK, Yamagata T (2020) Predictability of the super IOD event in 2019 and its link with El Niño Modoki. Geophys Res Lett. https://doi.org/10.1029/2019GL086713
Evensen G (2003) The Ensemble Kalman Filter: theoretical formulation and practical implementation. Ocean Dyn 53:343–367. https://doi.org/10.1007/s10236-003-0036-9
Griffies SM (2012) Elements of the Modular Ocean Model (MOM). GFDL Ocean Group, Technical Report No. 7, NOAA/Geophysical Fluid Dynamics Laboratory, Princeton, USA, 620 pp.
Griffies SM, Gnanadesikan A, Dixon KW et al (2005) Formulation of an ocean model for global climate simulations. Ocean Sci 1:45–79
Hu Z-Z, Kumar A, Huang B et al (2014) Prediction skill of North Pacific variability in NCEP climate forecast system version 2: impact of ENSO and beyond. J Clim 27:4263–4272. https://doi.org/10.1175/JCLI-D-13-00633.1
Jin EK, Kinter JL, Wang B et al (2008) Current status of ENSO prediction skill in coupled ocean–atmosphere models. Clim Dyn 31:647–664. https://doi.org/10.1007/s00382-008-0397-3
Kanamitsu M, Ebisuzaki W, Yang S-K et al (2002) NCEP-DOE AMIP-II REANALYSIS (R-2). Bull Amer Meteor Soc 83:1631–1644
Kim H-M, Webster PJ, Toma VE, Kim D (2014) Predictability and prediction skill of the MJO in two operational forecasting systems. J Clim 27:5364–5378. https://doi.org/10.1175/JCLI-D-13-00480.1
Kumar TSV, Krishnamurti TN, Fiorino M, Nagata M (2003) Multimodel superensemble forecasting of tropical cyclones in the pacific. Mon Wea Rev 131:574–583. https://doi.org/10.1175/1520-0493(2003)131%3c0574:MSFOTC%3e2.0.CO;2
Liang X, Li Q, Wu T (2022) Dynamical seasonal prediction of the asian summer monsoon in the China meteorological administration climate prediction system version 3. Front Earth Sci 10:934248. https://doi.org/10.3389/feart.2022.934248
Liu X, Wu T, Yang S et al (2015) Performance of the seasonal forecasting of the Asian summer monsoon by BCC_CSM1.1(m). Adv Atmos Sci 32:1156–1172. https://doi.org/10.1007/s00376-015-4194-8
Liu H, Tang Y, Chen D, Lian T (2017) Predictability of the Indian Ocean Dipole in the coupled models. Clim Dyn 48:2005–2024. https://doi.org/10.1007/s00382-016-3187-3
Liu B, Su J, Ma L et al (2021a) Seasonal prediction skills in the CAMS-CSM climate forecast system. Clim Dyn 57:2953–2970. https://doi.org/10.1007/s00382-021-05848-z
Liu X, Yao J, Wu T et al (2021b) Development of coupled data assimilation with the BCC climate system model: highlighting the role of sea-ice assimilation for global analysis. J Adv Model Earth Syst. https://doi.org/10.1029/2020MS002368
Luo J-J, Masson S, Behera S, Yamagata T (2007) Experimental forecasts of the Indian Ocean dipole using a coupled OAGCM. J Clim 20:2178–2190. https://doi.org/10.1175/JCLI4132.1
Luo J-J, Zhang R, Behera SK et al (2010) Interaction between El Niño and Extreme Indian Ocean Dipole. J Clim 23:726–742. https://doi.org/10.1175/2009JCLI3104.1
Reynolds RW, Rayner NA, Smith TM et al (2002) An improved in situ and satellite SST analysis for climate. J Clim 15:1609–1625. https://doi.org/10.1175/1520-0442(2002)015%3c1609:AIISAS%3e2.0.CO;2
Saji NH, Goswami BN, Vinayachandran PN, Yamagata T (1999) A dipole mode in the tropical Indian Ocean. Nature 401:360–363. https://doi.org/10.1038/43854
Shi L, Hendon HH, Alves O et al (2012) How predictable is the Indian Ocean Dipole? Mon Weather Rev 140:3867–3884. https://doi.org/10.1175/MWR-D-12-00001.1
Ummenhofer CC, England MH, McIntosh PC et al (2009) What causes southeast Australia's worst droughts? Geophys Res Lett 36:L04706. https://doi.org/10.1029/2008GL036801
Wang G, Cai W, Yang K et al (2020) A unique feature of the 2019 extreme positive Indian Ocean dipole event. Geophys Res Lett 47:e2020GL088615. https://doi.org/10.1029/2020GL088615
Webster PJ, Moore AM, Loschnigg JP, Leben RR (1999) Coupled ocean–atmosphere dynamics in the Indian Ocean during 1997–98. Nature 401:356–360. https://doi.org/10.1038/43848
Winton M (2000) A reformulated three-layer sea ice model. J Atmos Oceanic Technol 17:525–531. https://doi.org/10.1175/1520-0426(2000)017%3c0525:ARTLSI%3e2.0.CO;2
Wu T, Yu R, Zhang F et al (2010) The Beijing Climate Center atmospheric general circulation model: description and its performance for the present-day climate. Clim Dyn 34:123–147. https://doi.org/10.1007/s00382-008-0487-2
Wu T, Yu R, Lu Y et al (2021) BCC-CSM2-HR: a high-resolution version of the Beijing Climate Center Climate System Model. Geosci Model Dev 14:2977–3006. https://doi.org/10.5194/gmd-14-2977-2021
Yang K, Cai W, Huang G et al (2020) Oceanic processes in Ocean temperature products key to a realistic presentation of positive Indian Ocean dipole nonlinearity. Geophys Res Lett. https://doi.org/10.1029/2020GL089396
Zhao S, Jin F, Stuecker MF (2019) Improved predictability of the Indian Ocean dipole using seasonally modulated ENSO forcing forecasts. Geophys Res Lett 46:9980–9990. https://doi.org/10.1029/2019GL084196

Publisher's Note